Faculty of Science

Department of Physics

Energy level alignment at polymer:fullerene-metal interfaces

Thesis in partial fulfilment for the

Degree of Bachelor of Science with Honours in Physics

Edwin Tan Yu Hang

A0071997L

Supervisors: Assoc. Prof. Peter Ho, Dr. Png Rui-Qi

7 April 2014

Acknowledgement

This work would not have been possible without the guidance and help of several individuals who in one way or another contributed and extended their valuable assistance in the preparation and completion of this study.

First and foremost, I would like to express my upmost gratitude to Dr.Png Rui Qi for her constant guidance, patience, encouragement and for sharing her wealth of knowledge with me.

I am extremely grateful to Associate Professor Peter Ho and Assistant Professor Chua Lay Lay for accepting me into this dynamic research group and for the all the interesting and enriching discussions that we had.

I would also like to thank Dagmawi for helping to fix the helium compressor and Meng How for being a great friend.

Last but not least, the rest of ONDL members who helped in one way or another. Thank you for making my duration in ONDL a wonderful experience!

Abstract

State-of-the-art organic solar cells typically have an active layer made up of a conjugate polymer donor and a fullerene acceptor. For the optimization of the cell performance, it is important to understand how energy alignment at organic-electrode interfaces affect the open circuit voltage (V_{oc}) and thus the power conversion efficiency (PCE) of the cell. This report systematically investigates the energy level alignment at fullerene – metal interfaces through device built-in potential (V_{bi}) measurements so as to understand contact effects in organic solar cells. V_{bi} of (6, 6)-phenyl C61 butyric acid methyl ester (PCBM) and indene-C60 bisadduct (ICBA) devices with 5 different metal cathodes (Ag, Al, Au, Ca and Cu) were obtained by Electroabsorption spectroscopy (EA). EA spectroscopy avoids the problem of thickness dependent Fermi level pinning seen in the ultraviolet photoelectron spectroscopy (UPS) technique. Furthermore it allows measurement to be conducted in device configuration providing the advantage of directly relating EA results to device performance. The effective work function of Ag, Al, Au, Ca and Cu on PCBM are measured to be 3.95eV, 3.80eV, 4.15eV, 3.60eV and 3.85eV respectively while the effective work function of Ag, Au, Ca and Cu on ICBA are measured to be 3.55eV, 4.00eV, 3.45eV and 3.95eV. Fourier transform infra-red spectrometry (FTIR) measurements showed indications of Ca and Al charge transfer doping of C60 fullerene in PCBM which sets the Fermi level at metal-fullerene interfaces.

List of figures

List of tables

Contents

Introduction

Organic solar cells have attracted increasing attention as a renewable energy source in recent years due to their potential low-cost compared to traditional silicon based solar cells[1], as well as their ease of fabrication, simple device structure, promising applications in light-weight, large-area devices and their possibility to flex, roll, fold for portability[1-3].

The PCE of organic solar cells have improved from less than 1% in 1995[4] to almost 5% in the in the one of the most representative poly (3-hexylthiophene) (P3HT): (6, 6)-phenyl C61 butyric acid methyl ester (PCBM) system in 2005[5], to more than 10% in device with novel architecture[6]. However, the PCE of organic solar cell is still low compared to it inorganic counterparts. Zhao et al reported PCE of 24.4% in monocrystalline silicon solar cell in 1998[7] and recently Sharp Corporation developed a concentrator triple-junction compound solar cell with PEC of 44.4%[8]. For organic solar cells to be a viable alternative, more investigation is required in understanding the factors affecting PCE of organic solar cells.

1.1 Organic semiconductor

Organic semiconductors can be classified into two major classes, small molecules and polymers. Both have π-conjugated systems in which single and double carbon-carbon bonds alternates throughout the polymer or small molecule. In double carbon-carbon bonds, the first bond is a σ bond forms the backbone of the polymer or small molecule, while the second bond are π bonds which are formed from the over lapping p_z orbitals of sp^2 hybridized carbon atoms (Figure 1). The overlap of p_z orbitals between adjacent carbon atoms form π orbital that are delocalized over the molecule or along the segments of the polymer chain. The filled π orbital form the valence states while the empty π^* orbital form the conduction states. Increasing the number of alternating single and double bonds will lead to the formation of quasi continuous energy “bands”. The highest occupied molecular orbital (HOMO) and

lowest unoccupied molecular orbital (LUMO) in organic semiconductor are analogous to the valence band and conduction band respectively in inorganic semiconductors. The HOMO-LUMO gap in organic semiconductor is analogous to the energy band gap in inorganic semiconductors (Figure 2). The typical band gap in organic semiconductor ranges from 1ev to 3ev[9].

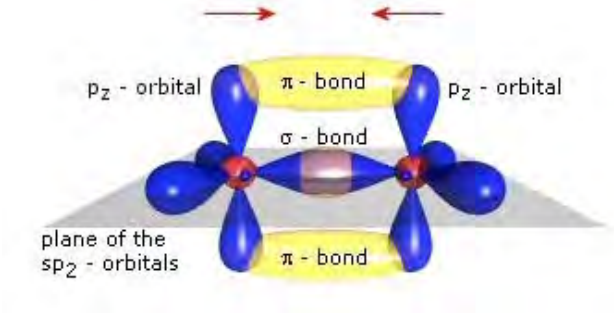

Figure 1: Formation of pi-conjugated systems from sp_2 hybridized orbitals

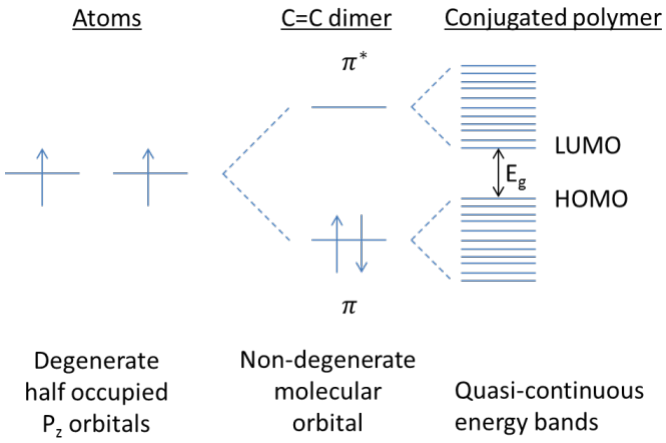

Figure 2: Schematic energy diagram showing the effects of repeated energy level splitting in conjugated polymers. When two sp2 carbon atoms approach each other, their pz orbitals split into bonding and anti-bonding molecular $\boldsymbol{\pi}$ orbitals. When a large number of pz orbitals overlap, quasi-continuous bands form with a "band" gap

1.2 Organic solar cell device structure

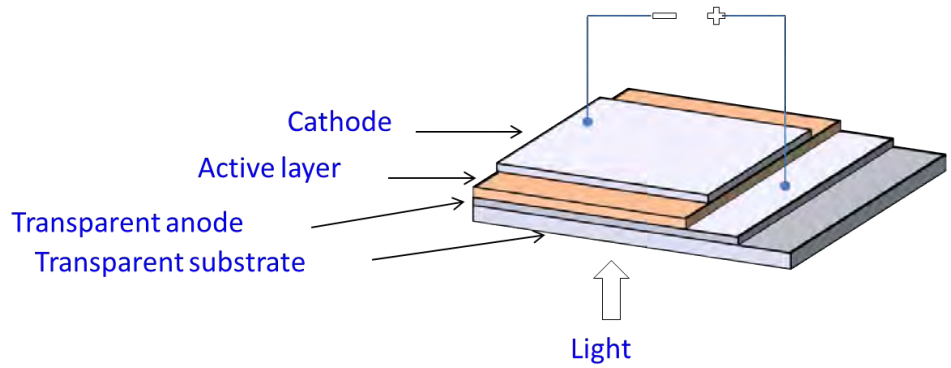

Figure 3: Device structure of a basic organic solar cell consist of a transparent substrate and anode, an active layer and a cathode.

Organic solar cells consist of a transparent substrate, transparent anode, active layer and a top cathode arranged in the configuration shown in Figure 3. In organic solar cell research, glass substrates are frequently used due to its low cost and stability. Alternatively, flexible plastic substrates such as poly(ethylene) terephthalate (PET) can be used in fabricating flexible organic solar cell devices[10].

The transparent anode used in current organic solar cells is a transparent conducting oxide known as indium tin oxide (ITO). ITO is a highly degenerate n-type semiconductor which is preferred for its high work function, conductivity and transmittance in the visible light spectrum. The work function of ITO can be varied over a wide range between about 3.7ev to 5.1ev by controlling the oxygen stoichiometry through surface cleaning, treatments and preparation techniques. Carbon residues on ITO surfaces are known to lower its work function whereas treatments with oxidizing agents such as oxygen plasma raise its work function[11].

ITO anode is typically coated with a thin layer of conductive polymer to function as hole injection layer to reduce hole injection barrier between the active layer and ITO. One of the commonly used conductive polymer is poly(3,4-ethylenedioxythiophene):poly(styrenesulphonic acid) also known as PEDT:PSSH. PEDT:PSSH has a work function of 5.2ev which provides better hole injection properties

than ITO hence it helps to achieve better match between the energy levels of the anode and the HOMO of the donor. In addition, PEDT:PSSH also doubles as a buffer layer to ITO's surface roughness and provide a surface with more well defined work function.

The earliest active layer in organic solar cells consist of a single layer of organic material and have been proven to have very low efficiency. A significant improvement in organic solar cell design came in 1986 when Tang et el[12] discovered that higher efficiencies can be obtained by utilizing bi-layer organic solar cells where donor and acceptor layers in the active layer are spatially separated, in analogy to the classical p-n junction. A significant drawback of this design is the short exciton diffusion length of the organic material limits the thickness of the donor and acceptor layers which leads to weak absorption. If the active layer is too thick, the exciton generated too far away from the heterojunction may recombine before reaching the heterojunction. One of the most important breakthroughs in the field of organic solar cells is the development of bulk heterojunction (BHJ) concept[4]. In BHJ organic solar cells, the acceptor is distributed more homogeneously into the donor matrix to form an interpenetrating network of acceptors and donors, thereby generating a three dimensional network of donor-acceptor interfaces for more effective exciton dissociation, which ultimately led to higher photoinduced charge generation. A typical active layer comprises a solution blend of conjugated polymer and small molecules, usually a fullerene. P3HT:PCBM blend is the most commonly used and well optimized active layer for organic solar cells. P3HT:PCBM organic solar cells exhibits high device efficiency and due to its consistency and ease of fabrication, P3HT:PCBM organic solar cell has became an important model for investigating various device parameters in organic solar cells.

A low work function metal is deposited onto the active layer via thermal evaporation to form the top cathode. Low work function metal such as calcium or lithium is used so as to form ohmic contact with the underlying organic active layer. Such metals are highly unstable in ambient environment due to their high reactivity[13] hence an additional metal layer such as Aluminum is often deposited over the reactive metal to protect it from oxidizing.

1.3 Operational principles of organic solar cells

Photocurrent generation in an organic solar cell consist of 4 steps (a) exciton generation (b) exciton diffusion (c) exciton dissociation and (d) charge collection. When an incident photon is absorbed by the active layer in the organic solar cell, an electron in the active layer is excited from the HOMO to the LUMO leaving a hole behind in the HOMO. Due to low dielectric constant and localized electron and hole wave function in organic semiconductor, columbic attraction exist between the electron-hole pair. The resulting electron-hole pair is called a Frankel exciton with binding energy of 0.1-1.4 eV[14].

Under the influence of the internal electric field gradient, exciton diffuses towards the donor-acceptor interface where exciton dissociation takes place. For effective dissociation to occur, the difference between the HOMO of the donor and the LUMO of the acceptor has to be lower than the potential difference minus the binding energy to make the transfer of an electron to the LUMO of the acceptor an energetically favorable process. A hole remains in the HOMO of the donor after an electron is transferred into the LUMO of the donor.

The hole and electron then drift under the influence of the internal electric field towards the active layer/electrodes interface where they are extracted. To achieve high charge extraction efficiency, potential barriers at active layer/electrode interfaces have to be minimized. Ideally, there should be ohmic contact between the active layer and electrode, where the work function of the anode matches the HOMO of the donor and the work function of the cathode matches the LUMO of the acceptor. The entire photocurrent generation process is depicted in Figure 4.

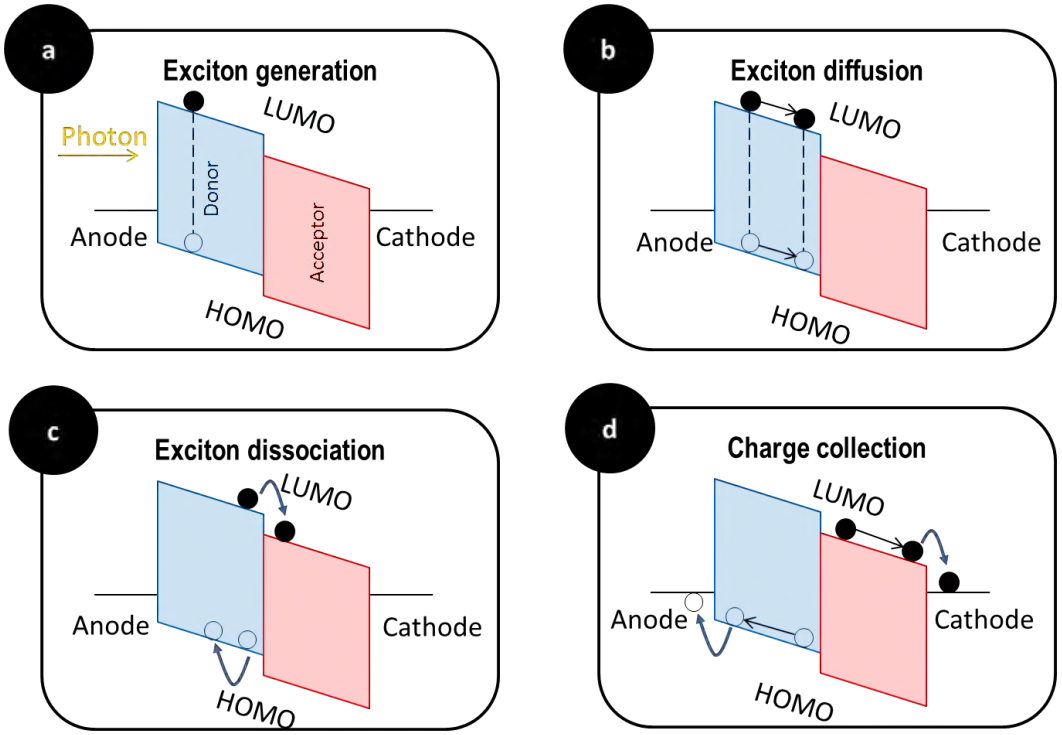

Figure 4: (a) Exciton generation: Donor layer absorbs photon and generates an electron-hole pair (b) Exciton diffusion: Electron-hole pair diffuses to the donor-acceptor interface under influence of internal electric field (c) Exciton dissociation: electron-hole pair dissociates at the donor-acceptor interface and (d) Charge collection: electron and hole are collected at the respective electrodes

1.4 Model polymer donors and small molecule acceptors

Poly(phenylene vinylene)s (PPV) and polythiophenes (PTs) are two kinds of classic conjugated polymers which are broadly used in organic solar cells as electron donors. Poly[2-methoxy-5-(3',7'-dimethyloctyloxy)-1,4-phenylenevinylene] (MDMO-PPV) Figure 5(c) and poly(3-hexylthiophene) (P3HT) (Figure 5(d)) are representatives of PPV-based materials and PT-based materials respectively. Fullerene and its derivatives are broadly used as electron acceptor materials in organic solar cells. The solubility of unsubstituted fullerene is quite poor, which limits its application in device fabrication process. Therefore, different substituents were introduced onto fullerene. PCBM (Figure 5(a)) which was first prepared by Hummelen and Wudl[15] in 1995, is commonly used as an electron acceptor in organic solar cells. PCBM is a derivative of the C60 Buckminster fullerene with a phenyl ring and an

ester side group. It offers advantages of having good solubility in organic solvent such as chlorobenzene, di-chlorobenzene, chloroform, higher electron mobility and affinity[16]. PCE of 2.5% has been recorded in MDMO-PPV:PCBM based solar cells[17]. However, the absorption edges of MDMO-PPV is at about 585 nm, corresponding to a band gap of approximately 2.12eV[18], and output current density of the solar cells based on them was limited due to the big mismatch between their absorption spectra and the solar irradiation spectrum. P3HT on the other hand exhibits lower band gap, broader absorption band and also better hole mobility than MDMO-PPV. The PCE of P3HT:PCBM based organic solar cells reached up to 4%-5%[19-23] by thermal treatment[22], solvent[21] and vapor annealing[20] as well as mixture solvent treatment[23]. However, PCBM has weak absorption in the visible region which limits its ability in harvesting light. V_{oc} is closely related to the difference between the LUMO energy level of the acceptor and the HOMO energy level of the donor[24]. As PCBM has a low LUMO energy level it resulted in lower V_{oc}. To overcome the limitations of PCBM, He et al[25] synthesized a new soluble C60 derivative indene-C60 bisadduct (ICBA) (Figure 5(b)). The LUMO energy of ICBA is 0.17ev higher than PCBM and demonstrated higher V_{oc} and power conversion efficiency (PCE) of 6.5% under the same conditions[26]. Since it was first synthesized in 2010, ICBA have been adopted and optimised by various groups as an alternative electron acceptor to PCBM[27-29].

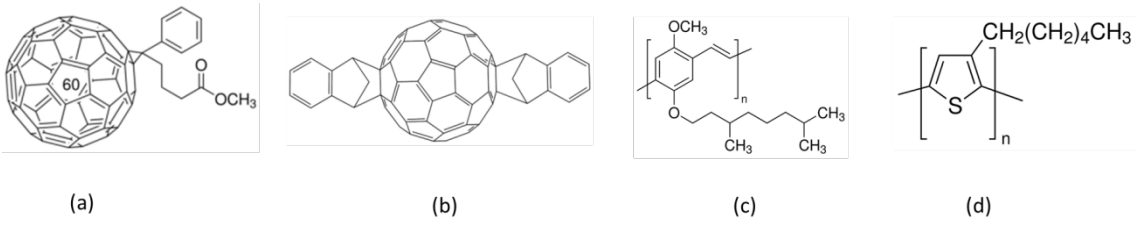

Figure 5: Chemical structure of fullerene acceptors (a) PCBM (b) ICBA and polymer donors (c) MDMO-PPV (d) P3HT

1.5 Energy level alignment at metal-semiconductor fullerene interfaces

1.5.1 Push back effect

Experimental work[30, 31] and theoretical studies[32, 33] have showed that weak physisorption of atoms or molecules on atomically clean metal in the absence of charge transfer can alter the work function of these metals.

The work function of metals depends on the bulk chemical potential and the electrostatic potential across the metal surface. The bulk chemical potential will not be affected by weakly physisorption atoms or molecules, but the electrostatic potential across the metal surface will. Figure 6(a) shows the charge density distribution of metal. The positive charge density created by the atomic nuclei can be described by the jellium model as a positive uniform background charge which end shows a step-like behavior as it drops from a constant value inside the metal to zero at the interface[34]. However the negative charge density due to electrons 'leaks' out of the surface forming a small density of negative charges on the surface of the metal[35]. The charge imbalance led to the formation of a metal-surface dipole.

Figure 6(b) shows a schematic energy diagram for the same metal substrate depicted in Figure 6. Φ_{SUB} is the work function of the metal substrate which is measured from the Fermi level E_F to the outer electrostatic potential energy ϕ^{out} outside the metal surface. ϕ^{in} is the inner electrostatic potential energy, μ is the bulk chemical potential of the metal and $\Delta\phi$ is the metal-surface dipole energy which is the difference between ϕ^{out} and ϕ^{in}.

When atoms or molecules are physisorbed on the surface of the metal, the electron-density tail at the metal surface is being compressed back into the bulk which reduces the metal-surface dipole potential $\Delta\phi$, the work function decreased by the same amount. Such was observed by Crispin et al when they tabulated the change in work function with respect to the change in metal-surface dipole for

Xenon physisorbed on various metals[36]. The effect which led to the decrease in work function is known as the push back effect.

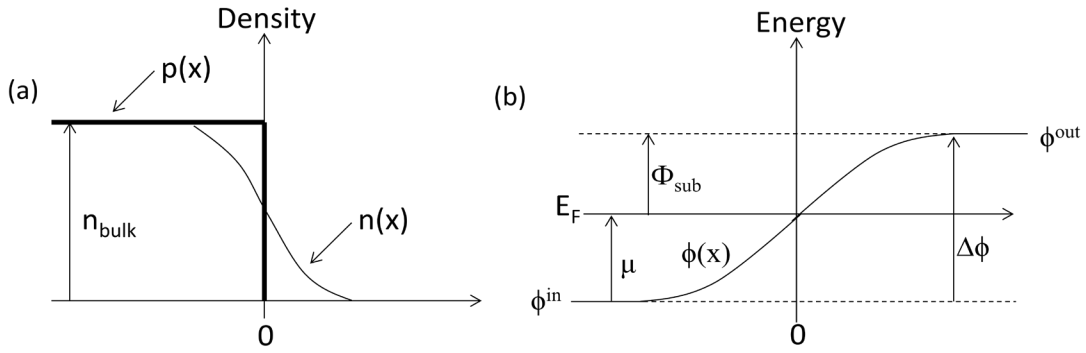

Figure 6: (a) Charge distribution at metal surface: p(x) is the positive charge due to atomic nuclei and n(x) is the negative charge due to electrons (b) Various relevant energies which contributes to work function of the substrate

1.5.2 Integer Charge Transfer Model & Fermi level pinning

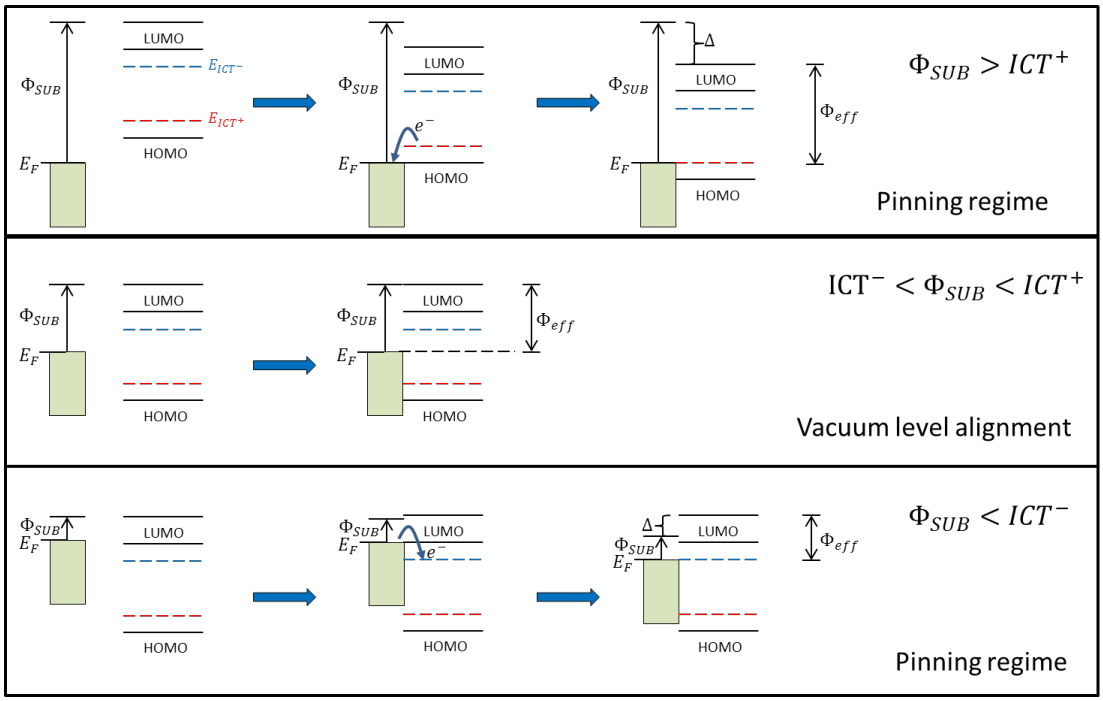

Figure 7: (Top) Fermi level pinning regime (Middle) Vacuum level alignment regime (Bottom) Fermi level pinning regime

Integer Charge Transfer (ICT) model[37] was used to describe energy level alignment across non-interacting metal-organic and organic-organic interfaces. According to the ICT model in Figure 7,

charge transfer only occurs via tunneling only if the surface work function of the metal substrates Φ_{sub} is greater (smaller) than the formation energy of positively (negatively) charged states E_{ICT+} (E_{ICT-}) in the organic material. Φ_{sub} used here is the work function of the metal substrate which has taken into account of the push back effect. Tunneling indicates the transfer of an integer amount of charge, one electron at a time, into well-defined charged states on the polymer or molecule. The energy of a positive (negative) ICT state E_{ICT+} (E_{ICT-}) defined as the energy required removing (add) one electron from the molecule/polymer producing a fully relaxed state.

Figure 7 (Top) illustrates the case where $\Phi_{sub} > E_{ICT+}$, that is the work function of the substrate is larger than the energy of the positive integer charge state of the organic material. When the organic material is brought into contact with the metal, electrons begins to flow from the surface of the organic material into the metal. As the flow continues, the organic interface becomes increasingly positively charged while the metal surface becomes increasingly negatively charged, this causes the formation of a metal-organic interface dipole that down-shifts the vacuum level. The potential continues to grow until equilibrium is reached, where the E_{ICT+} together with the potential energy Δ at the interface is equals to the substrate work function Φ_{sub}. At this point, no energy is gained or lost by transferring an electron to/from the organic material across the interface. Hence as long as $\Phi_{sub} > E_{ICT+}$, the resulting work function at equilibrium also known as the effective work function Φ_{eff} will be equal to E_{ICT+}, that is the Fermi level is pinned.

Figure 7 (Middle) illustrates the case where $E_{ICT-} < \Phi_{sub} < E_{ICT+}$. When the organic material is in contact with the substrate there will not be any spontaneous flow of electrons in either direction as it is not energetically favorable. Since no spontaneous charge transfer across the organic/substrate interface occurs in reaching equilibrium, there is no vacuum level offset, hence this is known as the vacuum level alignment regime. The effective work function Φ_{eff} is the same as the substrate work function Φ_{sub}.

Figure 7 (Bottom) illustrates the case where $\Phi_{sub} < E_{ICT-}$, that is the work function of the substrate is smaller than the energy of the negative ICT state of the organic material. When the substrate and organic material is in contact, electrons will spontaneously being to flow from the substrate into the organic material. The organic materials at the interface becomes increasingly negatively charged while the substrate becomes increasingly positively charged creating a potential at the interface which up-shifts the vacuum level. When the system reaches equilibrium, the effective work function Φ_{eff} will be equal to E_{ICT-} that is the Fermi level is pinned to the negative ICT state at the interface.

If one sweeps the substrate work function Φ_{sub} over a large enough range, a "mark-of-zorro" type dependence between Φ_{eff} and Φ_{sub} should be obtained as seen in Figure 8. It is worth noting that a full "Z" variation plot is rarely observed in most other organic semiconductor-metal bilayer systems [38-40]mainly because the E_{ICT+} - E_{ICT-} energy gaps of many OSCs are often larger than the degree of variation in Φ_{sub} achievable in practice.

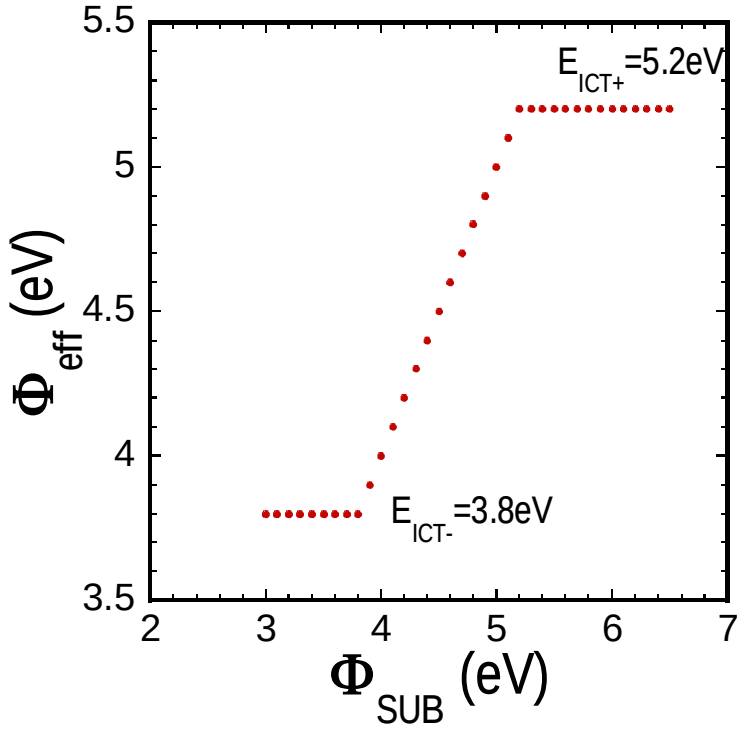

Figure 8: General $\boldsymbol{\Phi_{eff}}$ vs $\boldsymbol{\Phi_{SUB}}$ dependence predicted by the ICT model

1.6 Power conversion efficiency of organic solar cells

The power conversion efficiency of organic solar cells is given as

$$\eta = \frac{P_{out}}{P_{in}} = \frac{J_{MP} * V_{MP}}{P_{in}} = \frac{FF \cdot J_{SC} \cdot V_{OC}}{P_{in}}$$

The short circuit current density (J_{sc}) refers to the current measured when the device is connected in a short circuit. It has been shown that the J_{sc} is sensitive to the solvent type, film morphology and deposition method[41]. The formation of BHJ has led to enhancement of J_{sc} due to the increase in charge separation interfaces. However the J_{sc} for organic devices is still much lower than its inorganic counter parts. This is mainly due to spectral mismatch between the absorption spectrum of the active layer and the sunlight as well as the low carrier mobility in organic materials[42]. The fill factor (FF) refers to the ratio of the maximum power obtainable over the product of the J_{sc} and V_{oc}

$$FF = \frac{J_{MP} * V_{MP}}{J_{SC} * V_{OC}}$$

where the theoretical maximum would be 1. A FF nearer to 1 would also signify a steep gradient for the JV curve near the V_{oc}, indicating that most of the charge carriers would have already been extracted under the influence of a small electric field, hence suggesting a high efficiency in photocurrent extraction out of the device.

The open circuit voltage (V_{oc}) refers to the voltage of the device when there is no current flowing through, it also indicates the maximum possible voltage of the device. The V_{oc} has been suggested to vary linearly with energy gap between the HOMO band edge of the donor and the LUMO band edge of the acceptor, subjected to a loss of a few tenths of an eV, often thought to be 0.3eV[43, 44]. However, a number of electrical parameters of the cells are not known accurately, including the relevant electronic energies, and so it is not possible to be certain about the magnitude of this offset[45].

The V_{bi} is dependent on the difference between the anode and cathode work function

$$V_{bi} = \frac{\Phi_{anode} - \Phi_{cathode}}{e}$$

And the V_{oc} is related to the built-in potential V_{bi} by the following equation

$$V_{oc} = V_{bi} - \Delta$$

where Δ is the offset voltage required to balance the photocurrent against the injection current. Hence, the position of the Fermi levels of the electrodes will determine the V_{oc} which in turn affects the PCE of the organic solar cell.

The dependence of V_{bi} on cathode and anode work function indicates that the V_{oc} hence the PCE can be potentially limited by the Fermi level pinning effects mentioned in section 1.5.2. Such limitations to the V_{oc} was observed by Barbec et al[24] when they measured the V_{oc} of MDMO-PPV/PCBM organic solar cells with 4 different top metal cathodes -Ca, Ag, Au, Al-. where the work function of these metal cathodes ranged from 2.87eV to 5.1eV. The corresponding change in V_{oc} is less than 200mV despite varying the cathode work function by almost 2.2eV.

1.7 Motivation

To understand energy alignment and pinned Fermi levels at metal-organic interfaces a conventional technique is to utilize UPS technique to probe the interface of interest. Xu et al[46] and Braun et al[39] utilized this method to study pinned Fermi levels of PCBM and P3HT by spin coating the organic materials on variety of different substrates with work function that varies over a large range. UPS was utilized and the pinned levels of PCBM and P3HT were established to be at 4.3eV and 3.9eV respectively. However due to strong distance dependent polarization energy of the polaron measured in UPS, the Fermi level pinning depth is dependent on the thickness of the organic material. Only the first monolayer of the organic material gives the true Fermi level pinning relative to its band edges[47]. Moreover, UPS does not allow interfaces to be studied in device configuration.

For the design of future solar cells, it is important to understand how energy alignment at fullerene-metal interfaces affects the V_{oc} Built-in voltage V_{bi} is a more fundamental parameter and hence a natural starting point to understand the factors that limits the V_{oc} and ultimately the PCE in high-performance organic solar cells. Measurement of V_{bi} through EA spectroscopy avoids the problem of thickness dependent Fermi level pinning seen in the UPS technique. Furthermore it allows measurement to be conducted in device configuration. This provides the advantage of relating EA results directly to device performance.

The purpose of this thesis is to systematically investigate the energy level alignment at fullerene – metal interfaces through device built-in potential measurements so as to understand contact effects in organic solar cells.

2 Device fabrication

2.1 Solution preparation

Polystryene (PS): PCBM in weight ratio of 1:1, 1:2 and 1:3 and PS:ICBA in weight ratio of 1:3 were prepared. PS, an insulating polymer is used as a substitution for electron donor polymer P3HT as interest of this thesis lies in studying the properties of PCBM and ICBA. PS serves as a binder to hold the PCBM or ICBA small molecule together and is spectroscopically silent in the PCBM and ICBA stark peak region, hence will not cause interferences to the EA measurements.

PS (Mw= 2200000) was purchased from Sigma Aldrich and dissolved in anhydrous chlorobenzene to form PS solution of 8mg/ml in concentration. PS solution was annealed at 80°C for 1 hour to ensure that all solid PS has dissolved. An appropriate amount of PS solution was added to ICBA (1-Material) and PCBM (Sigma Aldrich) to obtain the desired weight ratio. The blend was annealed at 80°C for 1 hour to ensure that the fullerene has dissolved. Both blends were subjected to the same annealing condition before usage.

2.2 Sample preparation for EA Spectroscopy

Commercially purchased single stripe ITO substrate with photoresist layer protecting the ITO surface were used in this experiment. The photoresist layer was removed and the ITO substrates are the subjected to SC1 cleaning to remove any residual organic materials that may be on the surface. A layer of 50nm thick PEDT:PSSH (1:6) was spin coated onto the ITO substrate. As PEDT:PSSH solution contains fine particles, the PEDT:PSSH was dispensed onto the substrate through a 0.45μm nylon filter to remove the particles before spin coating. The samples were annealed at 130°C for 15 min in the nitrogen glove box to remove excess water solvent.

An active layer (PS:PCBM or PS:ICBA) of 120nm was spin coated onto the PEDT:PSSH layer in the glove box and annealed at 130°C for 15 min to remove excess chlorobenzene solvent. Finally the

samples were loaded into an evaporator where the metal cathode was evaporated through an 8 pixel mask at high vacuum of $1e^{-6}$ Torr.

2.3 Sample preparation for FTIR

Intrinsic silicon substrates were used for FTIR measurements. The photoresist layer on intrinsic silicon substrates was removed and the substrates are subjected to oxygen plasma to remove any residual materials that were on the surface. PS:PCBM (1:3) and PS:ICBA (1:3) film were deposited onto the intrinsic silicon substrates through spin coating. The films were then annealed at 130°C for 15 min to remove excess chlorobenzene solvent. The samples were loaded into an evaporator where 15nm thick of calcium was evaporated.

3 Characterization Techniques

3.1 J-V Measurement

J-V measurements in this work were performed using Keithley 4200 Semiconductor Parameter Analyser and the data was collected using "KITE" software. J-V measurement requires two probes from analyser, one of the probes will be used as a cathode probe and the other as an anode probe and they will be attached to the cathode and anode of the device respectively. A forward voltage sweep followed by a reverse voltage sweep will be performed in both the forward and reverse bias regions. The current values for each corresponding voltage values will be recorded and plotted by the software.

3.2 Electroabsorption Modulated Spectroscopy

3.2.1 EA Theory

EA spectroscopy measures the normalized light transmittance through (or reflectance from) a sample which is subjected to excitation by an external electric field. The transmitted intensity of light I_t is expressed as:

$$I_t = I_0(1-R)^2 e^{-\alpha d}$$

Where R is the reflection coefficient, I_0 is the incident light intensity, α is the absorption coefficient of the material and d is the distance through the material that the light travelled.

The absorption and reflection coefficient is dependent on the electric field strength F. Hence when an electric field is applied across the organic material, the field-induced change of the transmitted light intensity $\frac{\partial I_t}{\partial F}$ is given by

$$\frac{\partial I_t}{\partial F} = -I_0 e^{-\alpha d}\left[d(1-R)^2\frac{\partial \alpha}{\partial F} + 2(1-R)\frac{\partial R}{\partial F}\right]$$

The normalized change in light transmittance can be derived by dividing the change in transmittance intensity $\frac{\partial I_t}{\partial F}$ with the unperturbed transmitted light intensity, I_t

$$\frac{\Delta T}{T} = \frac{\Delta I_t}{I_t} = -d\Delta\alpha + \frac{2}{(1-R)}\Delta R$$

Where $\Delta\alpha = \frac{\partial \alpha}{\partial F}$ and $\Delta R = \frac{\partial R}{\partial F}$

As an approximation, the second term can be neglected hence the normalized transmittance is given by

$$\frac{\Delta T}{T} = -\frac{\Delta R}{R} \approx -d\Delta\alpha$$

The magnitude of the normalized transmittance or reflectance is dependent on the thickness of the material and the field-induced change in absorption coefficient.

The bulk polarization $\vec{P}$ of an organic macromolecule shows a linear response with electric field $\vec{F}$:

$$\vec{P} = \varepsilon_0 \cdot \chi \cdot \vec{F}$$

Where ε_0 is the vacuum permittivity and χ is the dielectric susceptibility which quantifies the degree of polarization of a dielectric material in response to an applied electric field.

The linear dependence of polarization on electric field strength is only valid over a limited range of light intensity. When the material is subjected to intense light illumination or strong electric field, dipoles are introduced in the material causing the polarization $\vec{P}$ to vary non-linearly with $\vec{F}$:

$$\chi_{eff} = \chi^{(1)} + \chi^{(2)} \cdot F + \chi^3 \cdot F^2 + \cdots$$

$\chi^{(2)}$ disappears for materials with inversion symmetry such as fullerene small molecules[48, 49] and conjugated polymers[50, 51]. This is because when the direction of the electric field across the material

is changed, only the signs changed but the absolute value of $\vec{P}$ remains the same. The two equations are given as

$\overrightarrow{P_2} = \varepsilon_0 \cdot \chi^{(2)} \cdot \left(\vec{F}\right)^2$ and $-\overrightarrow{P_2} = \varepsilon_0 \cdot \chi^{(2)} \cdot \left(-\vec{F}\right)^2$

Since both equations have to hold through, it is only possible if $\vec{P} = 0$ and $\chi^{(2)} = 0$. As such the polarization for conjugated polymers or fullerenes can be written as

$$\vec{P} = \varepsilon_0 \cdot \chi_{eff} \cdot \vec{F} = \varepsilon_0 \cdot (\chi^{(1)} + \chi^{(3)} \cdot \vec{F}\vec{F}) \cdot \vec{F}$$

For the above equation to be useful, a correlation needs to be drawn between $\chi^{(3)}$ and $\frac{\Delta R}{R}$ measured in EA measurements. This can be achieved by considering the relationship between χ_{eff} and the relative dielectric constant ε_r of the material:

$$\varepsilon_r = 1 + \chi_{eff} = 1 + (\chi^{(1)} + \chi^{(3)} F^2)$$

The Maxwell relation is given by

$$\varepsilon_r = \varepsilon_{r,1} + i\varepsilon_{r,2} = N^2 = (n + ik)^2$$

Where N is the refractive index of the material, n is the real component of the refractive index while k is the extinction coefficient or also known as attenuation factor which measures the loss of energy of an electromagnetic wave while propagating through a material.

The real component of the dielectric constant is give as

$$Re(\varepsilon_r) = \varepsilon_{r,1} = n^2 - k^2$$

While the imaginary component is given as

$$Im(\varepsilon_r) = \varepsilon_{r,2} = 2nk$$

The variation of χ_{eff} with electric field F can be written as

$$\Delta\chi_{eff} = \chi_{eff}(F) - \chi_{eff}(0) = \chi^{(3)}F^2 = 2N\Delta N = \Delta\varepsilon_r$$

Using Maxwell's electromagnetic theory, the propagation of a plane electromagnetic wave along the x direction with velocity v through a material with refractive index N is given as

$$E = E_0\exp[i\omega\left(\frac{\mathrm{Nx}}{\mathrm{c}} - t\right) = E_0\exp[i\omega\left[\left(\frac{nx}{c} - t\right)\right]\exp\left(-\frac{\omega kx}{c}\right)$$

The last exponential term $\exp\left(-\frac{\omega kx}{c}\right)$ measures the attenuation factor k of the material, $\frac{c}{N}$ and x denotes the speed and distance of light propagation in the material. c is the speed of light in vacuum (when N=1).

The optical power P or illumination intensity I of light can be determined by the conductivity σ of the material and the electric field vector E of the light wave:

$$P = \sigma E^2$$

Therefore transmittance of a light wave (i.e. I_t/I_o) that propagates from the surface of a material (where x=0) with conductivity (σ) through its thickness (where x=d) is given by:

$$T = \frac{I_t}{I_0} = \frac{P(d)}{P(0)} = \frac{E^2(d)}{E^2(0)} = \exp\left[-\frac{2\omega kd}{c}\right]$$

Where k is proportional to the material's absorption coefficient α and the wavelength of light λ by $\alpha = \frac{4\pi k}{\lambda}$. For molecular solids like conjugated polymers the equation can be expressed as

$$\alpha = \frac{4\pi k}{\lambda} = \frac{2\pi}{\mathrm{n}\lambda}Im(\varepsilon_r)$$

The change in absorption coefficient $\Delta\alpha$ is proportional to the imaginary component of the third order dielectric susceptibility $Im\chi^{(3)}$

$$\Delta\alpha \propto \Delta Im(\varepsilon_r) \propto Im\chi^{(3)}F^2$$

Hence

$$-\frac{\Delta T}{T} = \frac{\Delta R}{R} \approx d\Delta\alpha \propto Im\chi^{(3)}F^2$$

The above equation shows that A is a third order non-linear effect that exhibits quadratic dependence on applied electric field F.

3.2.2 Measurement of EA signals in organic semiconductors

EA measurements in multi-layered metal/polymer/metal sandwich structures were pioneered by Campbell et al[52, 53]. In this geometry, at least one of the electrodes needs to be transparent or semi-transparent for light to optically excite the organic semiconductor that is sandwiched between the two electrodes.

EA spectroscopy involves applying an electrical bias which comprise of a linear combination of DC and sinusoidal AC component $V = V_{dc} + V_{ac}Sin(\omega t)$ across the organic semiconducting layer. The total electric field in the organic semiconducting layer is

$$F = F_0 + F_{ac}\sin(\omega t)$$

Where F_0 is the DC field component and F_{ac} is the AC field component modulated at fundamental frequency (1ω). The EA response to a composite electric field is given as

$$\frac{\Delta R}{R}(hv) \propto Im\chi^{(3)}(hv)(F_0^2 + 2F_{ac}F_0\sin(\omega t) + F_{ac}^2[\frac{1-\cos(2\omega t)}{2}])$$

This shows that the electrical perturbation causes $\frac{\Delta R}{R}$ to be modulated at both fundamental and second harmonic (2ω) frequencies. The fundamental and second harmonic frequencies can be separately measured by employing a phase sensitive lock-in amplifier. The 1ω component of the EA signal is

$$\frac{\Delta R}{R}(hv) \propto 2Im\chi^{(3)}(hv)F_{ac}F_0 \sin(\omega t)$$

Where the DC field component F_0 is a linear combination of F_{bi} that arises from equibration of the electrodes' Fermi levels and $F_{dc}$the externally applied electric field. F_0 Is uniformly distributed along the thickness d of the organic semiconductor

$$F_0 = \frac{V_{bi} + V_0}{d}$$

Therefore the 1ω signal is given by

$$\frac{\Delta R}{R}(hv, \omega) \propto 2Im\chi^{(3)}(hv)V_{ac}(V_{dc} + V_{bi})$$

This equation indicates that the V_{bi} is simply the DC bias needed to null the 1ω EA signal.

From the microscopic view, the energy level E(F) of a state i in the electric field F is given by

$$E(F) = E(0) - m_i F - \frac{1}{2}(p_i F)F$$

Where m_i represents the dipole moment of the state and p_i is the polarizability. The energy shift ΔE of the optical transition from the initial state i to the final state f is therefore given by

$$\Delta E(F) = -(m_f - m_i)F - \frac{1}{2}(p_f - p_i)F^2$$

The first term gives the linear energy change from the different dipole moment of the initial state and the final state which averages out in the isotropic solid without permanent dipole. The second term describes the energy shift due to the polarizability difference of the initial state and the final state and is always present.

The absorption change from the external electrical field $\Delta\alpha$ can be expressed in terms of ΔE using the McLaurin series.

$$\Delta\alpha(hv) = \langle\frac{d\alpha}{dE}\Delta E\rangle + \frac{1}{2}\langle\frac{d^2\alpha}{d^2E}\Delta E^2\rangle$$

The only contribution on the first term comes from the quadratic stark effect $\frac{1}{2}\Delta pF^2$, while the isotropic averaging of $\langle(\Delta mf)^2\rangle$ in the second term would not average out but yield $\frac{1}{3}(\Delta mF)^2$ in the randomly distributed matrix. A third contribution comes from the oscillator transition to the former forbidden state in the presence of the electric field which is also quadratic in F.

The field induced change is absorption $\Delta\alpha$ can therefore be rewritten in terms of linear and quadratic stark effects:

$$\Delta\alpha = a\alpha + \frac{1}{2}\Delta pF^2\frac{\partial\alpha}{\partial E} + \frac{1}{6}\Delta mF^2\frac{\partial^2\alpha}{\partial^2 E}$$

3.2.3 Electroabsorption Spectroscopy Rig Setup

The schematic of the EA rig is shown in Figure 9. A device is loaded into the temperature-controllable cryostat and the pressure in the cryostat is lowered to 10^{-6} Torr using a turbo-molecular pump system backed by a dry diaphragm pump. The cryostat is connected to a helium compressor through pressurised helium supply and return lines. The cryostat was then cooled down to 30K before measurements are taken. A modulated drive voltage $V=V_{dc}+V_{ac}Sin(\omega t)$ generated by a signal generator within the lock-in amplifier is applied to the device during the measurement.

White light is produced by a 50 W quartz-tungsten-halogen lamp and is focused onto a monochromator (Newport CS260, F/3.9). The monochromatic light is collected by reflecting mirrors and focused onto the device in the cryostat through a glass window. Monochromatic light illuminated the device through the transparent glass/ITO anode at an angle of 45°. After travelling through the organic layers of the device, light is reflected off the shiny metal cathode at the back of the device and exits the cryostat through another glass window and is collected by a photodiode (Burr Brown, OPT301 M), the voltage is sent into the lock-in amplifier (Stanford Research SR830) and a digital multi-meter (Keithley 2400). The

digital multi-meter measures the DC reflectance (R) of the sample whereas the lock-in amplifier measures the change in reflectance (ΔR) that is induced by the applied modulating AC bias. The data collection process is automatically controlled by a home-made program written using Labview software. The two signals are processed a computer and the final output is the $\frac{\Delta R}{R}$ ratio.

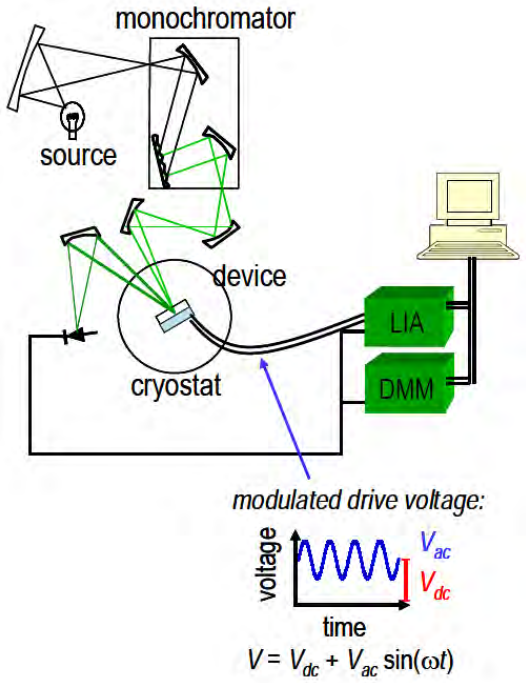

Figure 9: EA rig setup

3.3 Fourier Transform Infra-Red Spectrometry

Fourier Transform Infrared (FTIR) spectroscopy is a spectroscopic technique used to determine the chemical functional groups in a sample. Different functional groups absorb characteristic frequencies of IR radiation. Using various sampling accessories, FTIR spectrometers can accept a wide range of sample types such as gases, liquids, and solids. Thus, FTIR spectroscopy is an important and popular tool for structural elucidation and compound identification.

At temperatures above absolute zero, all atoms in molecules are in continuous vibration with respect to each other. When the frequency of a specific vibration is equals to the frequency of the IR radiation, the molecule absorbs the radiation.

The FTIR spectrometer consists of 3 important components, the IR source, IR detector and an interferometer.

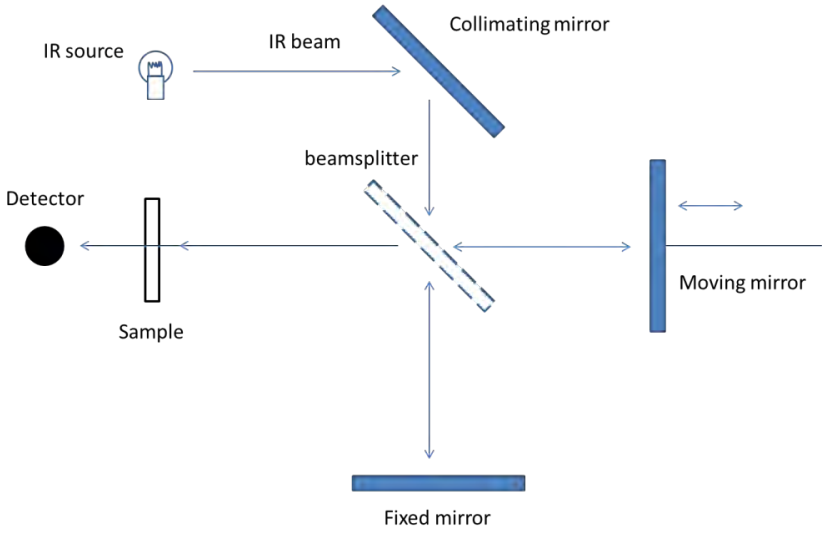

Figure 10: Components of a FTIR spectrometer

An IR beam comprising of a mid-range IR frequency was directed onto a collimating mirror which reflects the collimated beam onto a beam splitter. The beam splitter is a semi-reflecting device and is often made by depositing a thin film of germanium onto a flat KBr substrate. Half the IR beam that falls on the beam splitter is transmitted to the fixed mirror while the other half is reflected onto the moving mirror. Both beams are reflected from their respective mirrors and recombine at the beam splitter. As the moving mirror changes position, an interference pattern is formed. The resulting beam then passes through the sample and is focused at the detector. The constructive or destructive interference patterns may form depending on the optical path difference between the beam splitter and the two mirrors. The two light beams will be in phase with each other when their optical path difference δ is multiple of their wavelength λ, as follows:

$$\delta = n\lambda$$

Where $n = 0,1,2..(integers)$

The graph of the light intensity verse optical path difference is called an Interferogram. For FTIR, many wavelength of IR beam is emitted by the source at the same time; the resulting Interferogram is the superposition of all Interferogram of individual wavelength. The spectrum can be obtained by performing a Fourier transform.

4 Results and Discussion

4.1 Composition dependence of device built-in potential

Device with PS:PCBM active layer of the following ratios 1:1, 1:3 and 1:4 were fabricated with Ca cathode to ascertain if built-in potential of device is dependent on composition of polymer:fullerene. Figure 11 shows the optical-near-infrared EA reflectance spectra at different V_{dc} for Ca cathode devices with varying PS:PCBM ratio of 1:1, 1:3 and 1:4 by weight. These spectra were collected at 30K to avoid complications due to bulk carrier injections. The EA spectra exhibits strong feature centered at 2.3eV that is attributed to the quadratic stark shift of high-lying charge-transfer absorption. The intensity of the 2.3eV feature scales linearly with V_{dc} (Figure 11 inset) and shows polarity inversion at 1.60±0.05V. At forward bias with, bleaching of the π-π* absorption band occurs, thus the V_{dc} of this cell is 1.60±0.05V. The results are in agreement with previous investigation conducted by our group[45].The V_{dc} for all 3 PS:PCBM ratio devices are 1.60±0.05V indicating that there is no composition dependence between PS:PCBM ratio of 1:1 to 1:4. Hence the EA measurements performed on PS:PCBM(1:3) and PS:ICBA(1:3) devices presented in the following sections of this thesis is also applicable to devices with polymer: fullerene ratio varying from 1:1 to 1:4.

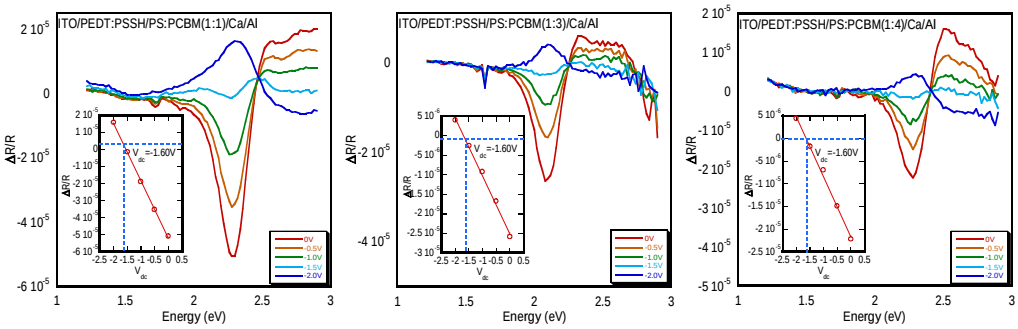

Figure 11: EA measurement for PS:PCBM(1:1), PS:PCBM(1:3) and PS:PCBM(1:4) calcium cathode device shows that built-in potential is not dependent on composition of PS:PCBM.

4.2 Temperature dependent JV characteristics

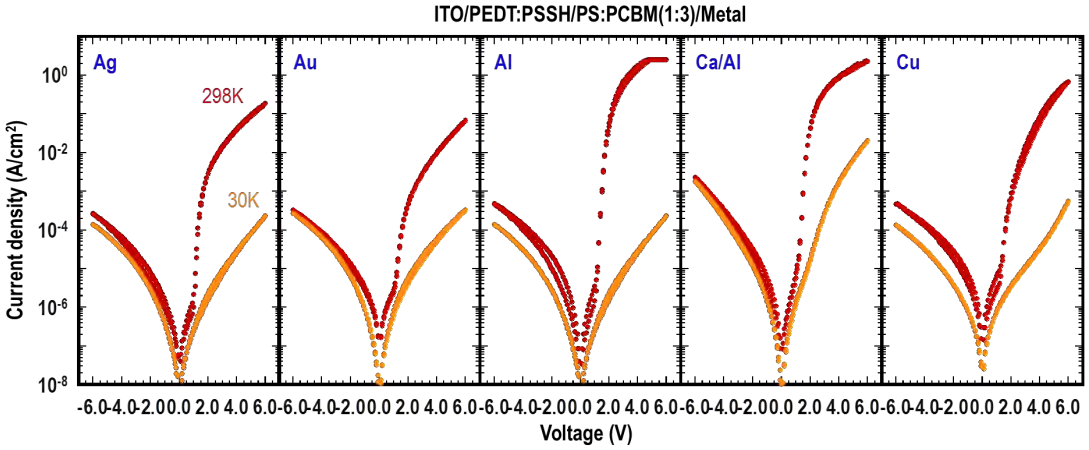

Figure 12: JV measurement for ITO/PEDT:PSSH/PS:PCBM(1:3)/Metal devices at 298K (red) and 30K (orange). Leakage current in forward bias regime at 30K indicates shut down of bulk carrier injection.

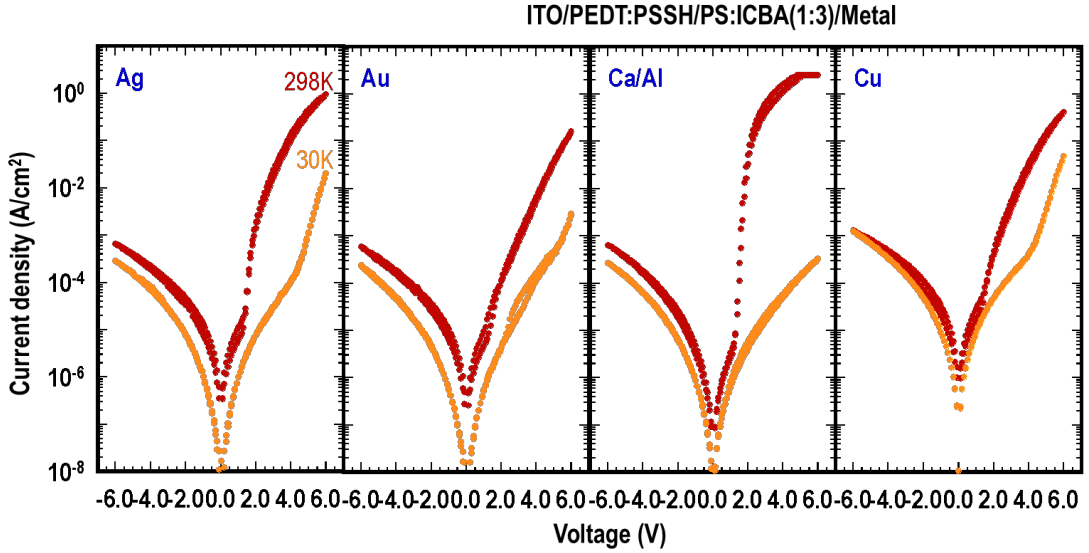

Figure 13: JV measurement for ITO/PEDT:PSSH/PS:ICBA(1:3)/Metal devices at 298K (red) and 30K (orange). Leakage current in forward bias regime at 30K indicates shut down of bulk carrier injection.

PS:PCBM(1:3) device with Al, Au, Ag, Ca and Cu cathode and PS:ICBA(1:3) device with Au, Ag, Ca and Cu cathode were fabricated. PS:fullerene in ratio of 1:3 was used to create an organic semiconductor-metal interface that is rich with PCBM or ICBA states. Higher fullerene ratios were not used as ICBA at higher concentration has solubility issues in chlorobenzene. JV measurement of

above mentioned devices were measured at 298K as shown in Figure 12 and Figure 13 . A voltage sweep was carried out from 0.0V to 6.0V back to 0.0V in the forward bias region and from 0.0V to -6.0V back to 0.0V in the reverse bias region. In the forward bias region, the kink between 1.0-2.0V in the 298K JV curves shown in Figure 12 and Figure 13 denotes the turn on voltage of the device at the given temperature. The turn on voltage is the minimum voltage required to acquire flatband condition in the device. The steep increase in current density after the device turn on voltage indicates bulk carrier injection from the electrodes into the LUMO of the PCBM (or ICBA). The JV curve in the reverse bias region denotes the leakage current of the device.

The devices were loaded into a Janis cryostat, the pressure in the cryostat was lowered to 10^{-6} Torr using a turbo-molecular pump system backed by a dry diaphragm pump. The cryostat was then cooled down to 30K by a helium compressor. JV measurement was taken again at 30K before the start of EA measurement to ensure proper electrode contacts and shut down of bulk carrier injection within the EA range of 0.0-2.0V, which may interfere with the EA measurements. PS:PCBM(1:3) devices with Ag,Au,Al cathodes have symmetrical JV curves at 30K, this shows that there is complete shutdown at 30K from 0.0-6.0V region and the measured current are solely due to leakage current. The rest of the devices such as PS:ICBA(1:3) with Cu cathode still show diode characteristics with turn on voltage at approximately 4.0V. Even though diode characteristics are not completely shut down in the measured range of 0.0-6.0V, the shift of the turn on voltage out of the 0.0-2.0V EA range is sufficient to reduce interference due to bulk carrier injections.

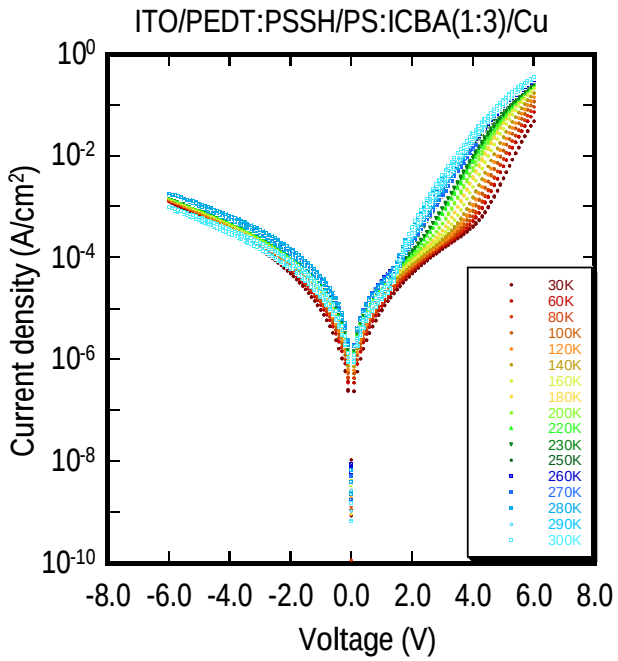

Figure 14: Temperature dependent JV measurement shows increase in turn on voltage and decrease in maximum current density as temperature decreases.

Temperature dependent JV measurement was taken for ITO/PEDT:PSSH/PS:ICBA(1:3)/Cu device. The PS:ICBA(1:3)/Cu device was placed in the cryostat and set to cool to a series of specific temperatures, showed in the legend of Figure 14 , before JV measurement was taken. It was observed that the current density and turn on voltage is dependent on temperature as shown in Figure 14 in the forward bias region, the kink at 1.5V in the 300K JV curve denotes the turn on voltage of the device at the given temperature. The steep increase in current density after the device turn on indicates bulk carrier injection from the electrodes. The current density at maximum voltage of 6.0V reaches $3\times10^{-1}Acm^{-2}$. As temperature decreases, the turn-on voltage shifts right towards higher value, from 1.5V at 300K to 4.1V at 30K, this indicates that it is now harder to inject carriers into the device. The curve between 0.0V to 4.1V now simply denotes the leakage current of the device. At the same time, the maximum current density at 6.0V decreases. The increase in turn on voltage and decrease in maximum current density is due to limited carrier concentration in the organic semiconductor layers.

4.3 Energy level alignment at metal-fullerene interface from EA spectroscopy

After JV measurements at 30K, EA spectra of the devices mentioned in section 4.2 were taken and plotted in Figure 16. The V_{bi} were extracted using the same method in section 4.1. Vacuum level alignment prevails at the PEDT:PSSH/PCBM contact due to the large ionisation potential of PCBM (6.1eV). The Fermi level of the pinned PS:PCBM(1:3)/Ca contact at flatband is 1.60eV above the Fermi level of PEDT:PSSH at 5.2eV. Hence the PCBM electron contact is pinned at 3.60±0.05eV as shown in the energy level diagram (Figure 15). The results are summarised in Table 1. Self-consistent energy level diagram can be constructed by taking the Fermi level of PEDT:PSSH as a reference (Figure 17).

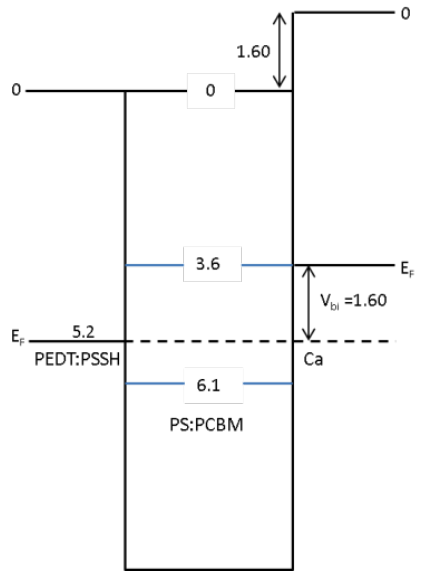

Figure 15: Energy level diagram for ITO/PEDT:PSSH/PS:PCBM/Ca device showed that the Fermi level of Ca is pinned to the LUMO of PCBM at 3.60eV.

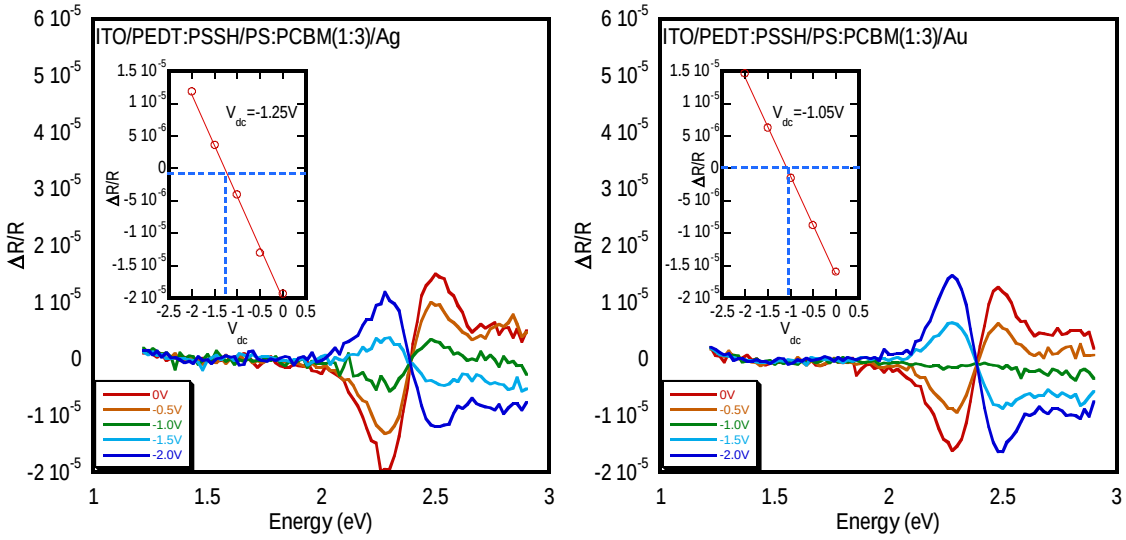
ITO/PEDT:PSSH/PS:PCBM(1:3)/Ag
ΔR/R
Energy (eV)
V_dc=-1.25V
V_dc
0V
-0.5V
-1.0V
-1.5V
-2.0V

ITO/PEDT:PSSH/PS:PCBM(1:3)/Au
ΔR/R
Energy (eV)
V_dc=-1.05V
V_dc
0V
-0.5V
-1.0V
-1.5V
-2.0V

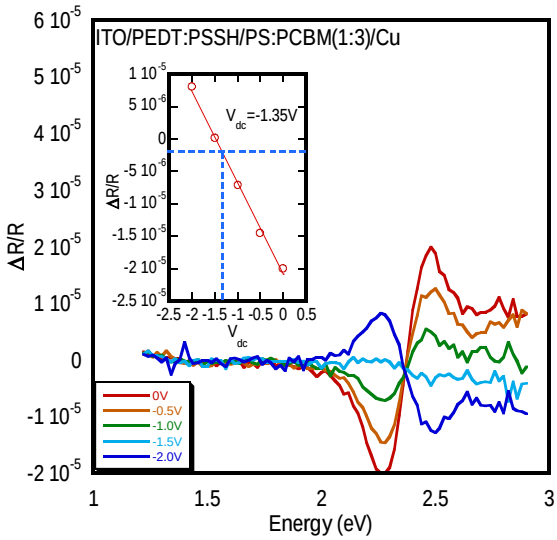
ITO/PEDT:PSSH/PS:PCBM(1:3)/Cu
ΔR/R
Energy (eV)
V_dc=-1.35V
V_dc
0V
-0.5V
-1.0V
-1.5V
-2.0V

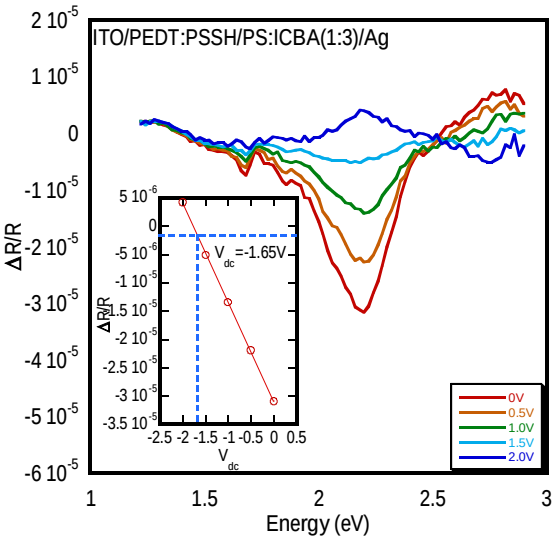
ITO/PEDT:PSSH/PS:ICBA(1:3)/Ag
ΔR/R
Energy (eV)
V_dc=-1.65V
V_dc
0V
0.5V
1.0V
1.5V
2.0V

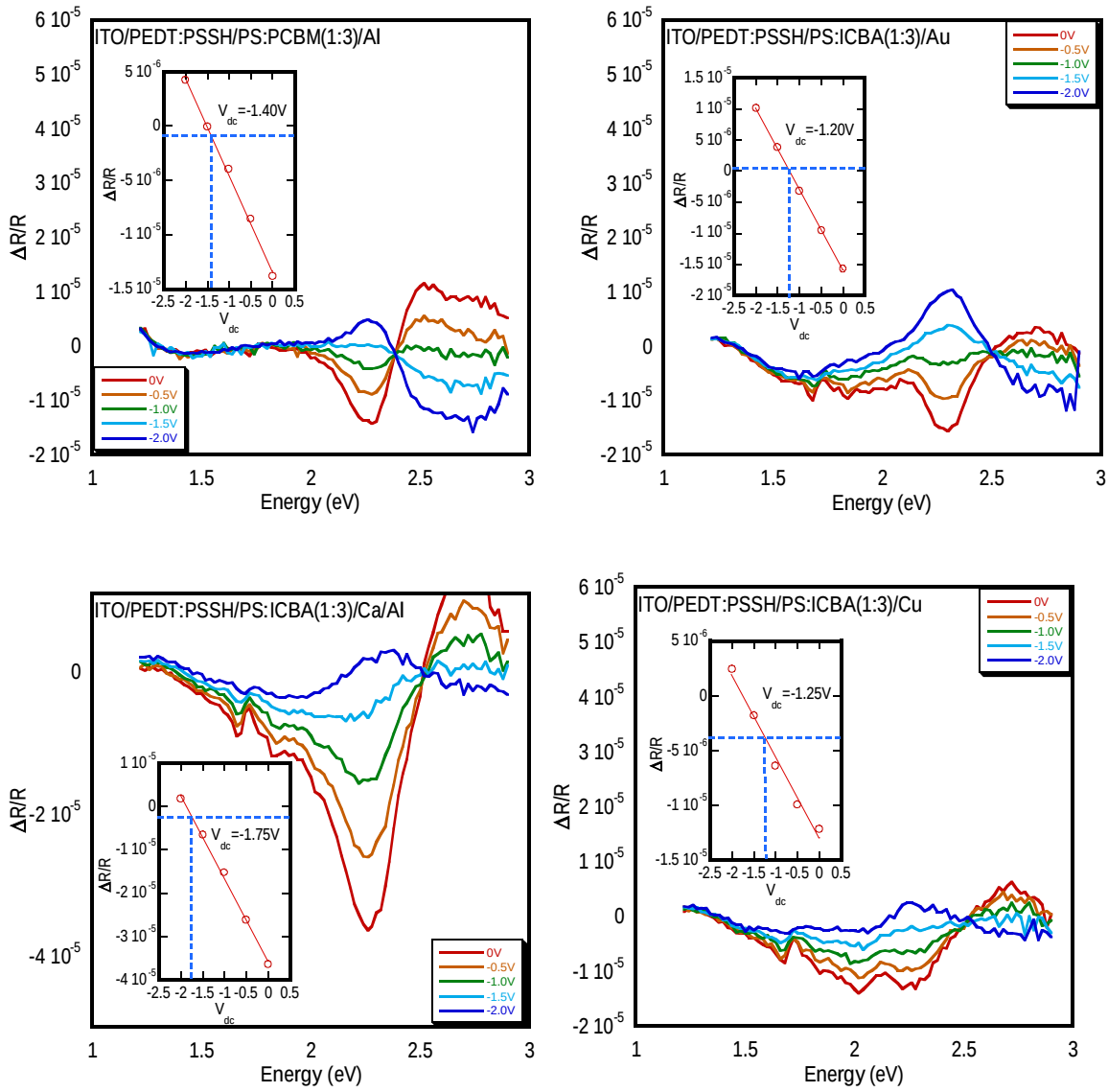

Figure 16: EA spectra of PS:PCBM(1:3) and PS:ICBA(1:3) devices

Metal	ϕ_{vac}(eV)	PS:PCBM(1:3)		PS:ICBA(1:3)	
		V_{bi} (V)	ϕ_{eff} (eV)	V_{bi} (V)	ϕ_{eff}(eV)
Ca	2.80	1.60	3.60	1.75	3.45
Al	4.20	1.40	3.80	-	-
Ag	4.40	1.25	3.95	1.65	3.55
Cu	4.70	1.35	3.85	1.25	3.95
Au	5.20	1.05	4.15	1.20	4.00

Table 1: Summary of vacuum work function, effective work function, built-in potential for PS:PCBM(1:3) and PS:ICBA(1:3) devices with varying top metal electrode

Figure 17: Energy level diagram for PS:PCBM(1:3), PS:ICBA(1:3), F8, TFB, F8BT and OC_1C_{10}-PPV devices with different metal electrodes

Al, Ag, Au and Cu in PS:PCBM(1:3) devices showed decrease in work function from 4.20eV, 4.40eV, 5.20eV and 4.70eV respectively to 3.80eV, 3.95eV, 4.15eV and 3.85eV respectively. While Ag, Au and Cu in PS:ICBA(1:3) device showed decrease in work function from 4.40eV, 5.20eV and 4.70eV respectively to 3.55eV, 4.00eV and 3.95eV respectively. In previous work by Zhou et al[54], EA spectroscopy was performed for the polymer organic semiconductors [2,5-dialkoxy-substituted poly(p-phenylenevinylene) (OC1C10-PPV), poly(9,9-dioctylfluoren-2,7-diyl) (F8), poly(9,9-dioctylfluorene-2,7-diyl-1,4-phenylene-(N-p-sec-butylphenyl) imino-1,4-phenylene) (TFB), or poly(9,9-dioctylfluorene-2,7-diyl-benzo-3,1,2-thiadiazole-4,7-diyl) (F8BT) sandwiched between PEDT:PSSH and various metal cathodes (Al, Au, Ag and Ca). The measured effective work function of Al, Au, Ag and Ca in the absence of Fermi level pinning in these polymers are 3.4±0.1eV, 4.4±0.1eV, 3.7±0.1eV, and 2.4±0.1eV. The decreases in work function of in these metals were attributed to push back effect described in section 1.5.1. However it is know that charge transfer is common at fullerene-metal

interfaces and can cause the fullerene to be doped, hence pinning the Fermi level of the metal. Metal doping of fullerene will be discussed in the next section.

Work function of Ca device increase from 2.8eV to 3.6eV in PS:PCBM(1:3) and to 3.45eV in PS:ICBA(1:3). In both cases, the Fermi level of calcium aligns 0.05eV away from the LUMO of the fullerene. Similar behaviour was also observed by Zhou et al [54], the work function of Ca increased from 2.8eV to 3.0eV when it is placed in contact with a π-conjugated polymer OC_1-C_{10}-PPV (Figure 17) and such increase was attributed to Ca Fermi level pinning to the electron polaron band found at the edge of the LUMO of the polymer.

4.4 FTIR evidence of doped PCBM

It is well known that C60 fullerene can be doped by reactive alkali metals such as lithium, sodium, potassium, rubidium and caesium[55, 56], by alkaline earth metal such as calcium[57], magnesium[58] and by transition metals such as copper[59, 60], silver[61] aluminium[62] and gold[63] to form either $C60^-$ or $C60^{2-}$.

FTIR measurements were performed on two separate PS:PCBM(1:3) films to ascertain if the PCBM was doped by Ca and/or Al. 100nm of PS:PCBM(1:3) film was spin coated onto oxygen plasma treated intrinsic silicon substrate and annealed at 130°C for 15 min in the glove box. The sample was loaded and sealed in a nitrogen chamber with KBr windows for the IR beams to pass through. The chamber was loaded FTIR machine and measurements taken in nitrogen atmosphere. The same sample was loaded into a thermal evaporator and 15nm of Ca (and Al) was evaporated onto the PS:PCBM(1:3) film at $1e^{-6}$ Torr. The Ca-doped film and Al-doped film were measured by FTIR again using the same procedure. Measurements in nitrogen atmosphere kept the film in inert environment to avoid contamination from air or moisture which can oxidize the metal or dedope the film. Since the same film was measured before and after evaporation, any changes in intensity, loss or appearance of peaks must be due to interaction with Ca (and Al).

FTIR measurements indicate that there was a decrease of C60 band at 1428cm^{-1} and increase of band at 1393cm^{-1} after doping. The change in bands at 1428cm^{-1} and 1393cm^{-1} is characteristic of the doping of C60 to form C60^{-}. Similar observations were made by C. Kvarbstrom et al[56] when they used alkali metals to dope C60. This showed that evaporating Ca onto PS:PCBM film has doped the fullerene.

Ca dopes PCBM by transferring its electron over to form PCBM-. The transferred electron is resides on the C60 molecule forming C60^{-} which gave rise to the decrease of band at 1428cm^{-1}and increase of band at 1393cm^{-1}. The Fermi level in PCBM had zero density of states in the undoped state. Doping of PCBM through electron transfer populated and set the Fermi level of PCBM at 3.60eV. The Fermi level of Ca is subsequently aligned with the Fermi level of doped PCBM, thus pinning it at 3.60eV.

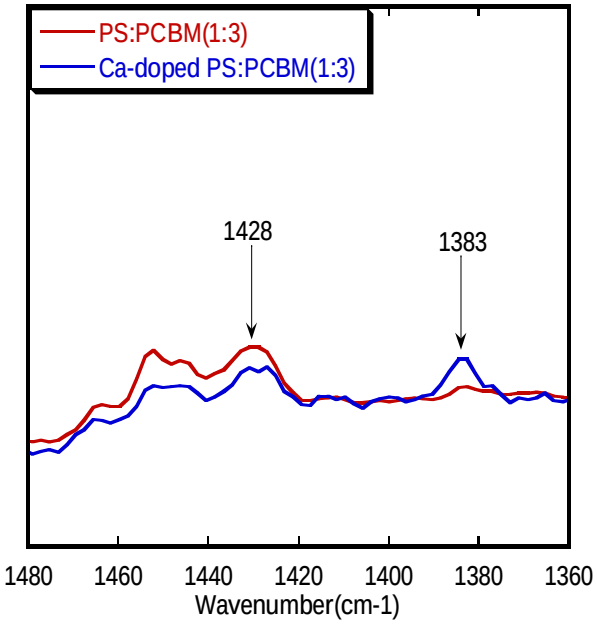

Figure 18:FTIR measurement of PS:PCBM and Ca-doped PS:PCBM film indicated that PCBM is successfully doped by Ca.

Similarly for Al-doped PS:PCBM(1:3) film, there is decrease of C60 band at 1428cm^{-1}and increase of band at 1393cm^{-1}indicating that Al has successfully doped the PCBM film as shown in Figure 19. Charge transfer from Al metal into C60 molecule in PCBM sets the Fermi level to be pinned at 3.80eV.

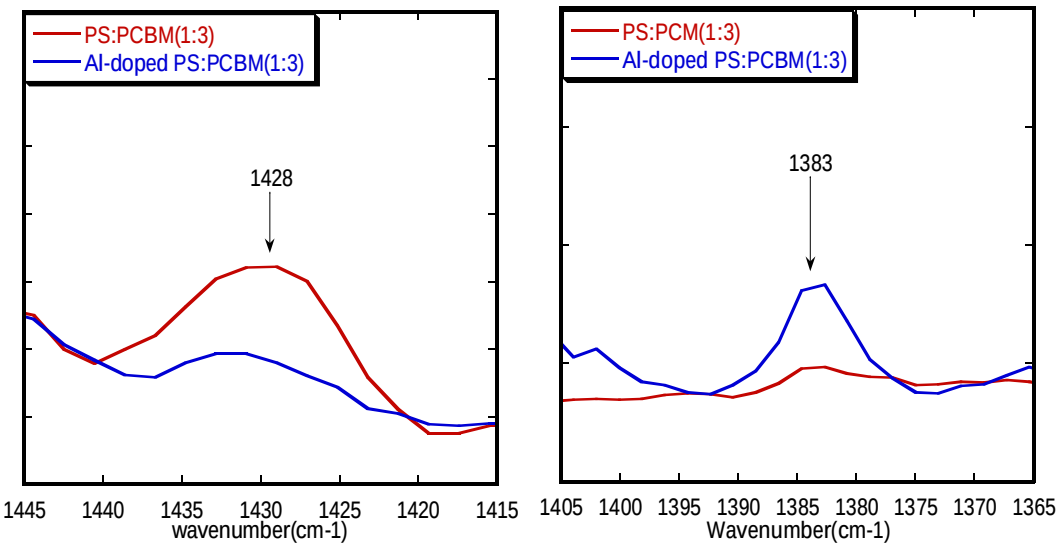

Figure 19: FTIR measurement for Al-doped PCBM indicates that there is decrease of 1428cm^{-1} band and increase in 1383cm^{-1} band indicating that PCBM has been doped by Al

Since electron transfer occurs between the C60 molecule and metal, the doping of PCBM and ICBA is largely independent on the side group. Hence, doping of C60 molecule is also expected for Ca, Cu, Al, Ag and Au on both PCBM and ICBA fullerene. The degree of doping is dependent on the work function of the metal. Metals with higher (lower) work function would contribute less (more) charge to each C60 molecule giving rise to different doping levels[60], hence the Fermi level of the organic layer varies based on the dopant metal it is in contact with. This is evident from Figure 17, Ca having the lowest work function contributes the most charge hence the Fermi level is pinned closest to the LUMO whereas Au which has the highest work function contributes the least charge hence Fermi level is pinned furthest away from the LUMO.

4.5 Effective work function and current injection properties of metal

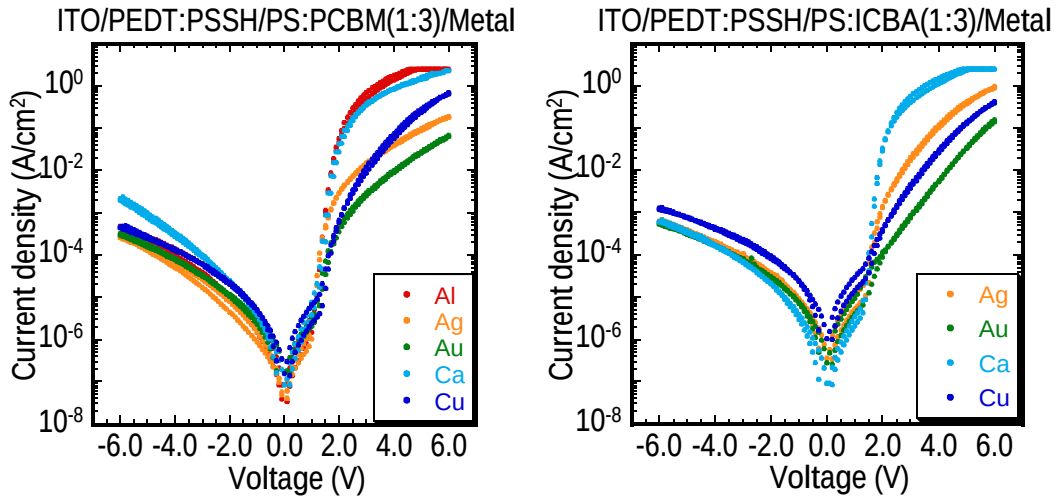

Figure 20: JV curves of (left) PS:PCBM(1:3) and (right) PS:ICBA(1:3) devices for Al, Ag, Au, Ca and Cu electrodes

The ability for EA spectroscopy to take measurements in device configuration provides the advantage of directly relating EA results to device performance. It is observed that the effective work function of metals obtained from EA spectroscopy is closely related to its current injection properties. In general, the closer the Fermi level of the metal is to the LUMO of the fullerene, the better the current injection. From Figure 17, the Fermi level of Ca is the closest to the LUMO of PCBM, followed by Al, Cu, Ag and Au being the furthest away. Comparing the sequence to Figure 20, it is observed that Ca and Al which are closest to the LUMO has the highest current density at 6.0V indicating that they have better current injection properties. Cu, Ag and Au follow in sequence. Similar observations can be made for PS:ICBA(1:3) device. The Ca device's Fermi level lies closest to the LUMO has the highest current density at 6.0V and Au with Fermi level furthest away has the lowest current density measured.

The correlation between work function and current injection is due to the current injection barrier which is the energy difference between the LUMO and the Fermi level of the metal cathode. For Ca devices, the Fermi level of Ca is pinned very closely to the LUMO forming near ohmic contact with the fullerene hence there is little current injection barrier. On the other end of the spectrum, Fermi level of Au is

furthest away from the LUMO hence there is large current injection barrier which explains the low current density in Au devices.

4.6 Fermi level pinning and PCE of organic solar cells

As described in section 1.6, the PCE of organic solar cell is dependent on the V_{oc} which is in turn dependent on the V_{bi} of the device. The V_{bi} of the device is determined by the difference between the effective work function of the anode and cathode. The effective work function of anode and cathode is affected by the push back effect and Fermi level pinning. The degree of push back effect and pinned Fermi levels varies for different metal and different fullerene, hence it is important to investigate pinned Fermi levels and push back effect that various fullerenes have on metals before deciding on suitable metal electrodes to use for optimising device PCE and other parameters.

One would thought that Ca cathode would make a much superior cathode than Ag cathode due to its low vacuum work function of 2.80eV compared to 4.40eV in Ag, however due to Fermi level pinning effects in Ca and Ag the effective work function for Ca and Ag in PCBM is 3.45eV and 3.55eV, only 0.1eV in difference compared to 1.6eV before. Even though Ca is still a slightly better cathode than Ag, Ag which is more stable in ambient condition can now be considered a viable alternative to Ca cathode with little lost in PCE.

Another example would be the case of Ag and Cu in PCBM device. The vacuum work function of Ag and Cu is 4.40eV and 4.70eV respectively. Ag would be a natural choice of better performing cathode since the vacuum workfunction is closer to the LUMO. However as due to charge transfer doping and pinning of Fermi level, the effective work function of Ag and Cu is 3.95eV and 3.85eV respectively. Cu now becomes a better cathode than Ag. Both of these examples serve to illustrate the importance of investigating the energy level alignment at metal-fullerene interface in order to optimise device performance.

5 Conclusion

EA spectroscopy was used to determine built-in voltage in PCBM and ICBA devices with Al, Au, Ag, Ca and Cu cathodes so as to study the contact effects at metal-fullerene interfaces. We have investigated the dependency of built-in voltage on PS:PCBM ratio and determined it to be independent of the composition over a the ratio range of 1:1 to 1:4. Temperature dependence of JV characteristics and shut down of bulk carrier injection was also discussed. The correlation between work function and current density was observed and was attributed to carrier injection barrier. Effective work function of metal in PCBM and ICBA were determined by EA spectroscopy and difference between vacuum work function and effective work function was attributed to Fermi level pinning due to metal doped fullerene interfaces. FTIR measurements showed that Al and Ca doped the C60 molecule in PCBM film hence pinning the Fermi level of Al and Ca. We have also illustrated that the effective work function of metal is an important consideration when designing high performing organic solar cell.

6 References

1. Krebs, F.C., T. Tromholt, and M. Jorgensen, *Upscaling of polymer solar cell fabrication using full roll-to-roll processing.* Nanoscale, 2010. 2(6): p. 873-886.
2. Larsen-Olsen, T.T., et al., *Simultaneous multilayer formation of the polymer solar cell stack using roll-to-roll double slot-die coating from water.* Solar Energy Materials and Solar Cells, 2012. 97(0): p. 22-27.
3. Kim, J.Y., et al., *Efficient Tandem Polymer Solar Cells Fabricated by All-Solution Processing.* Science, 2007. 317(5835): p. 222-225.
4. Yu, G., et al., *Polymer Photovoltaic Cells: Enhanced Efficiencies via a Network of Internal Donor-Acceptor Heterojunctions.* Science, 1995. 270(5243): p. 1789-1791.
5. Reyes-Reyes, M., K. Kim, and D.L. Carroll, *High-efficiency photovoltaic devices based on annealed poly(3-hexylthiophene) and 1-(3-methoxycarbonyl)-propyl-1- phenyl-(6,6)C61 blends.* Applied Physics Letters, 2005. 87(8): p. -.
6. You, J., et al., *A polymer tandem solar cell with 10.6% power conversion efficiency.* Nat Commun, 2013. 4: p. 1446.
7. Zhao, J., et al., *19.8% efficient "honeycomb" textured multicrystalline and 24.4% monocrystalline silicon solar cells.* Applied Physics Letters, 1998. 73(14): p. 1991.
8. *Sharp Corporation*. 2014; Available from: http://sharp-world.com/corporate/news/130614.html.
9. *Handbook of Conducting Polymers.* CRC Press, 2007.
10. Espinosa, N., et al., *Life cycle assessment of ITO-free flexible polymer solar cells prepared by roll-to-roll coating and printing.* Solar Energy Materials and Solar Cells, 2012. 97: p. 3-13.
11. Brumbach, M., et al., *Surface Composition and Electrical and Electrochemical Properties of Freshly Deposited and Acid-Etched Indium Tin Oxide Electrodes.* Langmuir, 2007. 23(22): p. 11089-11099.
12. Tang, C.W., *Two layer organic photovoltaic cell.* Applied Physics Letters, 1986. 48(2): p. 183-185.
13. Jørgensen, M., K. Norrman, and F.C. Krebs, *Stability/degradation of polymer solar cells.* Solar Energy Materials and Solar Cells, 2008. 92(7): p. 686-714.
14. Choy, W.C.H., *Organic Solar Cells Materials and Device Physics.* 2013.
15. Hummelen, J.C., et al., *Preparation and Characterization of Fulleroid and Methanofullerene Derivatives.* Journal of Organic Chemistry, 1995. 60.
16. Mikroyannidis, J.A., et al., *A Simple and Effective Modification of PCBM for Use as an Electron Acceptor in Efficient Bulk Heterojunction Solar Cells.* Advanced Functional Materials, 2011. 21(4): p. 746-755.
17. Shaheen, S.E., et al., *2.5% efficient organic plastic solar cells.* Applied Physics Letters, 2001. 78(6): p. 841-843.

18. Omer, B.M., *Optical Properties of Mdmo-Ppv and MDMO-PPV/ [6,6]-Phenyl C61-Butyric Acid 3-Ethylthiophene Ester Thin Films.* International Journal on Organic Electronics, 2013. 2(2): p. 1-7.

19. Kim, Y., et al., *A strong regioregularity effect in self-organizing conjugated polymer films and high-efficiency polythiophene:fullerene solar cells.* Nat Mater, 2006. 5(3): p. 197-203.

20. Zhao, Y., et al., *Solvent-vapor treatment induced performance enhancement of poly(3-hexylthiophene):methanofullerene bulk-heterojunction photovoltaic cells.* Applied Physics Letters, 2007. 90(4): p. -.

21. Li, G., et al., *High-efficiency solution processable polymer photovoltaic cells by self-organization of polymer blends.* Nat Mater, 2005. 4(11): p. 864-868.

22. Ma, W., et al., *Thermally Stable, Efficient Polymer Solar Cells with Nanoscale Control of the Interpenetrating Network Morphology.* Advanced Functional Materials, 2005. 15(10): p. 1617-1622.

23. Moulé, A.J. and K. Meerholz, *Controlling Morphology in Polymer–Fullerene Mixtures.* Advanced Materials, 2008. 20(2): p. 240-245.

24. Brabec, C.J., et al., *Origin of the Open Circuit Voltage of Plastic Solar Cells.* Advanced Functional Materials, 2001. 11(5).

25. He, Y., et al., *Indene-C60 Bisadduct: A New Acceptor for High-Performance Polymer Solar Cells.* Journal of the American Chemical Society, 2010. 132(4).

26. Zhao, G., Y. He, and Y. Li, *6.5% Efficiency of Polymer Solar Cells Based on poly(3-hexylthiophene) and Indene-C60 Bisadduct by Device Optimization.* Advanced Materials, 2010. 22(39): p. 4355-4358.

27. Chang, C.-Y., et al., *Enhanced Performance and Stability of a Polymer Solar Cell by Incorporation of Vertically Aligned, Cross-Linked Fullerene Nanorods.* Angewandte Chemie International Edition, 2011. 50(40): p. 9386-9390.

28. Cheng, F., et al., *Enhancing the performance of P3HT:ICBA based polymer solar cells using LiF as electron collecting buffer layer and UV–ozone treated MoO3 as hole collecting buffer layer.* Solar Energy Materials and Solar Cells, 2013. 110(0): p. 63-68.

29. Lin, S.-H., et al., *Influence of mixed solvent on the morphology of the P3HT:Indene-C60 bisadduct (ICBA) blend film and the performance of inverted polymer solar cells.* Organic Electronics, 2013. 14(1): p. 26-31.

30. Seki, K., E. Ito, and H. Ishii, *Energy level alignment at organic/metal interfaces studied by UV photoemission.* Synthetic Metals, 1997. 91(1–3): p. 137-142.

31. Hückstädt, C., et al., *Work function studies of rare-gas/noble metal adsorption systems using a Kelvin probe.* Physical Review B, 2006. 73(7).

32. Michaelides, A., et al., *Resolution of an Ancient Surface Science Anomaly: Work Function Change Induced by N Adsorption on W{100}.* Physical Review Letters, 2003. 90(24): p. 246103.

33. Bagus, P., et al., *Work Function Changes Induced by Charged Adsorbates: Origin of the Polarity Asymmetry.* Physical Review Letters, 2008. 100(12).

34. Lang, N.D. and W. Kohn, *Theory of Metal Surfaces: Charge Density and Surface Energy.* Physical Review B, 1970. 1(12): p. 4555-4568.

35. Lang, N.D. and W. Kohn, *Theory of Metal Surfaces: Work Function.* Physical Review B, 1971. 3(4): p. 1215-1223.

36. Crispin, X., et al., *Characterization of the Interface Dipole at Organic/ Metal Interfaces.* Journal of the American Chemical Society, 2002. 124(27): p. 8131-8141.

37. Braun, S., W.R. Salaneck, and M. Fahlman, *Energy-Level Alignment at Organic/Metal and Organic/Organic Interfaces.* Advanced Materials, 2009. 21(14-15): p. 1450-1472.

38. Osikowicz, W., M.P. de Jong, and W.R. Salaneck, *Formation of the Interfacial Dipole at Organic-Organic Interfaces: C60/Polymer Interfaces.* Advanced Materials, 2007. 19(23): p. 4213-4217.

39. Braun, S., et al., *Energy level alignment regimes at hybrid organic–organic and inorganic–organic interfaces.* Organic Electronics, 2007. 8(1): p. 14-20.

40. Braun, S. and W.R. Salaneck, *Fermi level pinning at interfaces with tetrafluorotetracyanoquinodimethane (F4-TCNQ): The role of integer charge transfer states.* Chemical Physics Letters, 2007. 438(4-6): p. 259-262.

41. Liu, J., Y. Shi, and Y. Yang, *Solvation-Induced Morphology Effects on the Performance of Polymer-Based Photovoltaic Devices.* Advanced Functional Materials, 2001. 11(6): p. 420-424.

42. Mihailetchi, V.D., et al., *Cathode dependence of the open-circuit voltage of polymer:fullerene bulk heterojunction solar cells.* Journal of Applied Physics, 2003. 94(10): p. 6849.

43. Scharber, M.C., et al., *Design Rules for Donors in Bulk-Heterojunction Solar Cells—Towards 10 % Energy-Conversion Efficiency.* Advanced Materials, 2006. 18(6): p. 789-794.

44. Gadisa, A., et al., *Correlation between oxidation potential and open-circuit voltage of composite solar cells based on blends of polythiophenes/ fullerene derivative.* Applied Physics Letters, 2004. 84(9): p. 1609.

45. Liu, B., et al., *Evaluation of Built-In Potential and Loss Mechanisms at Contacts in Organic Solar Cells: Device Model Parameterization, Validation, and Prediction.* Advanced Energy Materials, 2014. 4(4): p. n/a-n/a.

46. Xu, Z., et al., *Energy level alignment of poly(3-hexylthiophene): [6,6]-phenyl C[sub 61] butyric acid methyl ester bulk heterojunction.* Applied Physics Letters, 2009. 95(1): p. 013301.

47. Zhao, L.-H., et al., *Polarization effects on energy-level alignment at the interfaces of polymer organic semiconductor films.* Applied Physics Letters, 2012. 101(5): p. 053304.

48. Wang, L.-S., et al., *Threshold photodetachment of cold C−60.* Chemical Physics Letters, 1991. 182(1): p. 5-11.

49. **Katsumi, Y., et al., *Marked Enhancement of Photoconductivity and Quenching of Luminescence in Poly(2,5-dialkoxy-p-phenylene vinylene) upon C 60 Doping.* Japanese Journal of Applied Physics, 1993. 32(3A): p. L357.**

50. **Liess, M., et al., *Electroabsorption spectroscopy of luminescent and nonluminescent π-conjugated polymers.* Physical Review B, 1997. 56(24): p. 15712-15724.**

51. **Cadby, A.J., et al., *Film morphology and photophysics of polyfluorene.* Physical Review B, 2000. 62(23): p. 15604-15609.**

52. **Campbell, I.H., M.D. Joswick, and I.D. Parker, *Direct measurement of the internal electric field distribution in a multilayer organic light-emitting diode.* Applied Physics Letters, 1995. 67.**

53. **Campbell, I.H., et al., *Direct Measurement of Conjugated Polymer Electronic Excitation Energies Using Metal/Polymer/Metal Structures.* Physical Review Letters, 1996. 76(11).**

54. **Zhou, M., et al., *Effective work functions for the evaporated metal/organic semiconductor contacts from in-situ diode flatband potential measurements.* Applied Physics Letters, 2012. 101(1): p. 013501.**

55. **Haddon, R.C., et al., *Conducting films of C60 and C70 by alkali-metal doping.* Nature, 1991. 350.**

56. **Kvarnstrom, C., et al., *An in situ spectrochemical study of the reduction of thin fullerene films.* Journal of Electroanalytical Chemistry, 2001. 511.**

57. **Wertheim, G.K., D.N.E. Buchanan, and J.E. Rowe, *Charge Donation by Calcium into the t1g Band of C60.* Science, 1992. 258.**

58. **Chikamatsu, M., et al., *Mg-doped C60 thin film as improved n-type organic semiconductor for a solar cell.* Applied Physics Letters, 2004. 84(1): p. 127-129.**

59. **Solodovnikov, S.P., *ESR studies of doping C60 fullerene by zinc, cadmium, copper, gallium, and indium vapors.* Russian Chemical Bulletin, 1997. 46(2): p. 289-291.**

60. **Hebard, A.F., R.R. Ruel, and C.B. Eom, *Charge transfer and surface scattering at Cu-C60 planar interfaces.* Physical Review B, 1996. 54(19).**

61. **Wertheim, G.K. and D.N.E. Buchanan, *Interfacial reaction of C60 with silver.* Physical Review B, 1994. 50(15): p. 11070-11073.**

62. **Yonehara, H. and C. Pac, *Dark and photoconductivity behavior of C60 thin films sandwiched with metal electrodes.* Applied Physics Letters, 1992. 61(5): p. 575-576.**

63. **Kuk, Y., et al., *Stressed C60 layers on Au(001).* Physical Review Letters, 1993. 70(13): p. 1948-1951.**